Importance of spinel reaction kinetics in packed-bed chemical looping combustion using a CuO/Al_2O_3 oxygen carrier

Chemical Engineering Journal 334 (2018) 1905–1916

Contents lists available at ScienceDirect

Chemical Engineering Journal

journal homepage: www.elsevier.com/locate/cej

Importance of spinel reaction kinetics in packed-bed chemical looping combustion using a CuO/Al_2O_3 oxygen carrier

M.A. San Pio, F. Sabatino, F. Gallucci*, M. van Sint Annaland

Chemical Process Intensification, Department of Chemical Engineering and Chemistry, Eindhoven University of Technology, P.O. Box 513, 5600 MB Eindhoven, The Netherlands

GRAPHICAL ABSTRACT

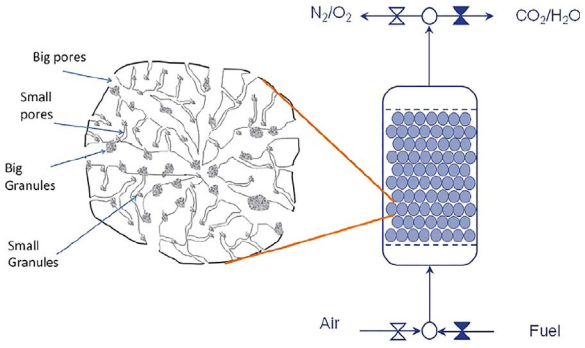

ARTICLE INFO

Keywords:
CO_2 capture
Chemical looping combustion
Cu-based oxygen carriers
Pressure redox kinetics

ABSTRACT

Chemical looping combustion is especially competitive for electrical power generation with integrated CO_2 capture when it is operated at high temperatures (1000–1200 °C) and high pressures (15 bar or higher). For these demanding conditions, dynamically operated packed bed reactors have been proposed, providing a good alternative to fluidized bed technology. This work addresses the importance of including the formation and reduction kinetics of spinel compounds to proper predict the packed bed reactor performance by validating a pseudo-homogeneous packed-bed reactor model to describe the redox kinetics of a CuO/Al_2O_3 oxygen carrier with experiments in a lab-scale packed bed reactor setup. A grain model describing the reaction kinetics of all solid species, including both spinel compounds ($CuAl_2O_4$ and $CuAlO_2$), was included in a particle model and used to develop correlations for the effectiveness factor as a function of the particle conversion in order to account for internal solids concentration profiles and mass transfer limitations. The particle effectiveness factors were subsequently included in the source terms of the component mass balances of the reactor model accounting for all the reactions of the spinel compounds. Cyclic experiments (oxidation with air and reduction with a H_2-N_2 mixture) have been carried out in a lab-scale packed bed reactor with a 12.5 wt% CuO/Al_2O_3 oxygen carrier at different temperatures ranging from 600 to 1000 °C. The experimental results are well described by the packed bed reactor model, only when including the developed particle effectiveness factors to fully account for the kinetics of the formation and reduction of the spinel compounds. The results confirm that it is neccesary to include a detailed description of the redox kinetics at the particle level to be able to accurately estimate the breakthrough time, cycle time, final amount of Cu present in the bed and the temperature rise in the reactor after reduction/oxidation reactions for packed-bed chemical looping combustion with a CuO/Al_2O_3 oxygen carrier.

* Corresponding author.
E-mail address: F.Gallucci@tue.nl (F. Gallucci).

https://doi.org/10.1016/j.cej.2017.11.138
Received 23 May 2017; Received in revised form 8 October 2017; Accepted 21 November 2017
Available online 24 November 2017

Nomenclature

CCS	carbon capture and storage
CLC	chemical looping combustion
TGA	thermogravimetric analyzer
TSCLC	two stage chemical looping combustion WGS water gas shift reaction

Symbols

b	stoichiometric factor in the reduction reaction of metal oxide, –
C	concentration, mol m^{-3}
C_p	heat capacity, J mol^{-1} K^{-1}
D_s	pre-exponential factor for diffusion, mol^{1-n} m^{3n-3} s^{-1}
$D_{s,0}$	pre-exponential factor for diffusion, m^2 s^{-1}
D_{ax}	axial dispersion coefficient, m^2 s^{-1}
d_{eff}	diffusive transport of gas phase components inside the particle, m^2 s^{-1}
d_p	particle diameter, m
E_A	activation energy, J mol^{-1}
EDs	activation energy, J mol^{-1}
ΔH_R	enthalpy of reaction, J mol^{-1}
k_0	pre-exponential factor, mol^{1-n} m^{3n-3} s^{-1}
k_x	solid diffusion decay constant, –
k_g	elements of mass transfer coefficient, kg mol^{-1}
M	molar mass, kg/mol
n	reaction order in gas, –
N_g	number of gaseous components, -
N_r	number of reactions, -
n_i	mass flux of component i, kg m^{-2} s^{-1}
n_{tot}	drift flux, kg m^{-2} s^{-1}
Nu	Nusselt number $= \alpha d_p/\lambda_{eff}$
p	pressure, Pa
Pe_{ax}	Heat Péclet axial number, -
Pr	Prandtl number, –
R	gas constant, J mol^{-1} K^{-1}
r	reaction rate, mol^{m-3} s^{-1}
r_g	grain radius, m
Re	Reynolds number, –
Sc	Schmidt number, –
T	temperature, K
t	time, s
v	superficial velocity, m s^{-1}
x	axial position, m
X	particle conversion, –
y	mole fraction in gas feed, –

Greek letters

α	heat transfer coefficient, W^{m-2} K^{-1}
ε	porosity, m^3 m^{-3}
ξ	stoichiometric factor, mol gas/mol solid
λ_{eff}	effective heat dispersion coefficient, W m^{-1} K^{-1}
η	effectiveness factor, –
η_g	Dynamic gas viscosity, kg m^{-1} s^{-1}
ω	mass fraction, kg kg^{-1}

subscripts

s	solid
g	gas
act	active
i	gas component
j	solid component
p	particle
red	reduction

superscripts

in	inlet
o	in oxidized state

1. Introduction

To reduce anthropogenic CO_2 emissions and combat climate change Chemical Looping Combustion (CLC) technologies have been proposed [1,2]. CLC technologies enable the combustion of a fuel via the consecutive reduction and oxidation of a supported metal/metal-oxide particle, referred to as oxygen carrier, to produce high temperature depleted air for electric power generation with facilitated CO_2 capture (for sequestration or further use in the context of Carbon Capture Utilization and Storage, CCUS). CLC has been shown to be very competitive with other technologies when operated at very high temperatures (1000–1200 °C) and high pressures (above 15 bar) and integrated with a combined cycle gas turbine [3–5]. Conventionally, interconnected fluidized bed reactors were proposed for CLC [6–11]. In this reactor concept, the particles are transported between an air reactor (typically a riser), where hot air is produced via the oxidation of the particles, and a regeneration unit (typically a bubbling fluidized bed), where the particles are reduced with methane or syngas while producing a concentrated CO_2 exhaust stream. With this reactor system, a continuous production of hot air is achieved without air/methane slip between the reactors [6]. However, the main drawbacks of this reactor concept are related to the transport of the oxygen carrier. Not only an additional energy input is required to transport the particles, but also a cyclone is required to separate the particles from the hot air stream. This particle separation is particularly difficult considering the required, extremely harsh process conditions (high pressure and very high temperature) and the fact that even fines (resulting from inevitable particle attrition in the fluidized bed reactors) need to be removed to protect the downstream gas turbine.

In view of the efficiency gains by operation at elevated pressures, dynamically operated packed bed CLC reactors [4,12,13], where the oxygen carrier is stationary and is alternately reduced and oxidized via periodic switching of the fuel and air streams, show promise because of their relative ease of operation at higher pressures in comparison to interconnected fluidized bed reactor systems [14]. A disadvantage of the packed bed system is that the oxygen carrier is thermally cycled between the temperature of the air feed (typically around 450 °C) and the maximum temperature (typically 1200 °C). This poses significant challenges on the oxygen carriers, which should have high redox reactivity at low temperature and high thermal, chemical and mechanical stability at high temperatures. To avoid this challenging high temperature cycling, Hamers et al. [15] investigated the possibility to carry out CLC in two packed bed reactors placed in series in a two-stage CLC (TSCLC) process. In this process, the temperature rise during the oxidation cycle is obtained in two consecutive stages, with each stage carried out in a different packed bed containing a different oxygen carrier. This alleviates the requirements on the selected oxygen carrier and reactor materials, while still achieving very comparable overall energy efficiencies [16].

Oxygen carriers are one of the most important elements of CLC technologies, as they determine to a large extent the overall process efficiency. In this work, the performance of a packed-bed CLC reactor is

investigated with special focus on a detailed description of the redox kinetics of the oxygen carrier. A CuO/Al_2O_3 particle has been selected as oxygen carrier, as it was previously shown to be very promising for packed-bed CLC because of its high reactivity at low temperatures, as long as the maximum temperature is limited because of the relatively low melting temperature of copper, and thus particularly suited as oxygen carrier material for the first stage of the TSCLC process [15]. In previous studies the redox kinetics of CuO/Al_2O_3 oxygen carrier materials have been studied [17–25]. This oxygen carrier, as well as many other oxygen carriers, shows a sharp decline in the particle conversion rate after typically 70–80% conversion (depending on the process conditions). Several researches have attempted to predict the redox kinetics with ad-hoc modification (such as using diffusion coefficients as a function of the particle conversion etc.) which are however not based on physical description of the prevailing phenomena. However, it has been elucidated that the reason for the slow-down in the redox reaction rate after a certain particle conversion was the formation and reduction of spinel compounds, which are phases formed due to the interaction of CuO with the support Al_2O_3. This has allowed to develop a particle model that can predict the redox kinetics for several oxygen carriers. In previous works [13,16], the integration of a particle model in a packed-bed reactor model has been shown, where the particle model describing the redox kinetics was a SCM based on an ad-hoc modification. This can only be valid for certain oprating conditions. As soon as the operating conditions vary, the fitting of the redox kinetics will not be valid anymore.

The novelty of this work is that we have developed a phenomenological kinetic model that describes the redox kinetics of supported CuO oxygen carriers (that can be further extended to other oxygen carriers such as FeO/Al2O3, NiO/Al2O3, etc.), based on the underlying chemistry, in particular the reduction reactions of the components formed by the interaction between the metal oxide with the support. The objectives of this paper are: i) to validate a 1D packed bed reactor model that accounts for all the reactions of spinel in the redox kinetics with experiments in a lab-scale packed-bed CLC reactor, ii) to show the importance of a proper description of the redox kinetics at the particle level to properly describe the packed-bed reactor behaviour, iii) to illustrate the importance of the formation and reduction of spinel compounds for a packed-bed CLC reactor at industrial conditions.

In a previous work an accurate description of the redox kinetics of the CuO/Al_2O_3 oxygen carrier has been developed using a pseudo-homogeneous grain model [26]. These kinetics have been integrated in a 1D packed-bed reactor model via correlation for the particle effectiveness factor as a function of the particle conversion, which were developed with a detailed particle model that accounts for intra-particle solids concentration gradients as well as internal (and external) mass transfer limitations of the gaseous species. Cycling experiments consisting of oxidation with air and reduction with a H_2-N_2 mixture have been carried out with CuO/Al_2O_3 as oxygen carrier in a lab-scale PBR setup in order to validate the reactor model that accounts for all the reaction kinetics of spinel. Finally, simulations with the extended packed-bed reactor model for a large scale reactor at industrial conditions have been carried out to demonstrate the importance of the spinel reduction in the particle model to proper describe the breakthrough times of the redox cycles at different temperatures, the temperature rise and the cycle time.

2. Materials and methods

Experiments have been carried out in a lab-scale packed bed reactor setup. The reactor is a U-shaped quartz tube (10 cm length and 0.7 cm diameter) where the temperature is controlled with an electrical oven. Inlet gas flow rates are controlled by mass flow controllers and after condensation of the produced steam the dry outlet gas composition is continuously analyzed with an in-line SICK gas analyzer. The setup is schematically represented in Fig. S.1 from the Supplementary Material.

Spherical particles of 12.5 wt% CuO/Al_2O_3 and 1.1 mm diameter (Sigma-Aldrich) were used as oxygen carrier. Upstream of the oxygen carrier inert quartz particles were positioned to heat the inlet gas to the desired reaction temperature.

During the experiments, the flow rate of the reactants was kept relatively low (200 ml/min) to obtain a reasonable breakthrough time.

Cycling experiments (oxidation with air and reduction with a H_2-N_2 mixture) were performed at different temperatures ranging from 600 °C up to 1000 °C, where the breakthrough times of the different reductant/oxidative gases were studied and used to validate a packed-bed reactor model described in the next section.

To further validate the model, several 'stop and check' experiments were carried out, where the reduction cycle was stopped at different moments in time to investigate which species were present in the oxygen carrier. Samples were taken from two different axial positions in the reactor, viz. at the entrance and at the middle of the oxygen carrier bed and the crystalline species were identified by X-ray diffraction in a Rigaku Mini-Flex 600 diffractometer at 298 K with a mobile copper anode.

3. Model description

The reactor model makes use of correlations for the particle effectiveness factors developed, which are developed with a particle model with detailed gas-solid kinetics, also referred to as the grain model. This grain model describes the gas-solid reactions on the scale of the grains in the particle, including in particular all the reactions of the spinel compounds, and is embedded in a particle model, that can account for the intra-particle multi-component molecular diffusion of the gas species in the pores of the porous particles (as well as multi-component external mass transfer limitations towards the particles, but this is unimportant in this work). For each gas-solid reaction an overall particle effectiveness factor as a function of the particle conversion is developed, which is subsequently integrated in the source terms of the component mass balances (and energy balance) of a pseudo-homogeneous packed-bed reactor model. The reason why the particle model has not been directly linked to the reactor model is the very large gain in computational efficiency. The reactor and particle model are described in more detail in the following sections. A schematic picture of how the models are linked to each other is provided in Fig. S.2 of the Supplementary Material.

3.1. Reactor model

The packed bed reactor is simulated with a one-dimensional pseudo-homogeneous (no temperature difference between particles and gas) plug flow reactor model with superimposed axial dispersion. In this model, no radial temperature and concentration gradients are considered. For the incorporation of the heat losses, it is assumed that the environment (oven) has a constant temperature and the amount of heat transferred from the reactor to the oven wall is evaluated using a constant heat transfer coefficient, α, taken from [23]. Table 1 shows an overview of the mass and energy balances. The axial mass dispersion and effective heat conductivity are described by the equations in Table 2. To solve the set of PDE's, a very efficient finite difference technique with higher order temporal and spatial discretization with local grid and time step adaptation is used [27]. In the next section, the mass and heat exchange between the gas phase and the oxygen carrier particle in described with a particle model. More details on the model and the numerical solution strategy are shown in Smit et al. [27] and Noorman et al. [4].

The initial time step is very small ($\Delta t_{min} < 1{\cdot}10^{-5}$ s) because significant accumulation and reaction in the porous particles is taking place… The time integration is performed with an implicit Singly For further details on the model, the accuracy, the validation of the higher order SDIRK schemes and the numerical method the interested reader is

Table 1
Mass and energy balances used in the model.

Component mass balances for the gas phase

$$\varepsilon_g\rho_g\frac{\partial\omega_{i,g}}{\partial t} = -\rho_g v_g\frac{\partial\omega_{i,g}}{\partial x} + \frac{\partial}{\partial x}(\rho_g D_{ax}\frac{\partial\omega_{i,g}}{\partial x}) + \varepsilon_g r_i M_i + \omega_{i,g}\sum_{j=1}^{N_g}\varepsilon_g r_j M_j$$

Component mass balance for the solid phase

$$\varepsilon_s\rho_s\omega_{act}^0\frac{\partial\omega_{s,j}}{\partial t} = \varepsilon_g r_j M_j$$

Energy balance (gas and solid phase)

$$(\varepsilon_g\rho_g C_{p,g} + \varepsilon_s\rho_s C_{p,s})\frac{\partial T}{\partial t} = -\rho_s v_g C_{p,g}\frac{\partial T}{\partial x} + \frac{\partial}{\partial x}(\lambda_{ax}\frac{\partial T}{\partial x}) + \varepsilon_g r_i\Delta H_{R,i} - \alpha\frac{4}{d_r}(T - T_{env})$$

Reaction rate

$$r_i = \varepsilon_{g,p}\eta k_0\exp(\frac{-E_A}{RT})C_{g,i}^n C_{s,j}^0$$

Momentum balance (Ergun equation)

$$-\frac{dp}{dx} = 150\frac{\eta_g v_g(1-\varepsilon_g)^2}{\varepsilon_g^3} + 1.75\frac{\rho_g v_g^2}{d_p}\frac{(1-\varepsilon_g)}{\varepsilon_g^3}$$

Table 2
Heat and mass dispersion descriptions.

Effective axial heat dispersion (Vortmeyer and Berninger) [28]

$\lambda_{ax} = \lambda_{bed,0} + \frac{\mathrm{RePr}\lambda_g}{\mathrm{Pe}_{ax}} + \frac{\mathrm{Re}^2\mathrm{Pr}^2\lambda_g}{6(1-\varepsilon_g)\mathrm{Nu}}\lambda_{bed,0}$ is calculated by the Bauer and Schlünder equation [29]

Gunn and Misbah equation [30]

$$\mathrm{Pe}_{ax} = \frac{2\left(0.17 + 0.33\exp[\frac{-24}{\mathrm{Re}}]\right)}{1-\left(0.17 + 0.33\exp[\frac{-24}{\mathrm{Re}}]\right)}$$

Gunn equation [31]

$$\mathrm{Nu} = (7-10\varepsilon_g + 5\varepsilon_g^2)(1-0.7\mathrm{Re}^{0.2}\mathrm{Pr}^{1/3}) + (1.33-2.4\varepsilon_g + 1.2\varepsilon_g^2)\mathrm{Re}^{0.2}\mathrm{Pr}^{1/3}$$

Axial mass dispersion [32]

$$D_{ax} = \left(\frac{0.73}{\mathrm{ReSc}} + \frac{0.5}{\varepsilon_g + \frac{9.7\varepsilon_g^2}{\mathrm{ReSc}}}\right)v_g d_p$$

where

$$Sc = \frac{\eta_g}{\rho_g d_{eff}},\ \mathrm{Re} = \frac{v_g\rho_g d_p}{\eta_g},\ \mathrm{Pr} = \frac{\eta_g \mathrm{Cp}}{\mathrm{kg}}$$

where d_{eff} is the maximum effective diffusivity of all the gas-phase components.

referred to our earlier work [4,27].

3.2. Particle model

The redox kinetics are described with a pseudo-homogeneous model taken from a previous work [26]. The reaction pathways are summarized in Fig. S.3 of the Supplementary Material. The redox reaction equations and the reaction rate expressions of the CuO/Al_2O_3, where the reaction rate constants follow an Arrhenius type temperature dependency, have been listed in Table 3 together with the pre-exponential reaction rate constants and activation energies.

The low activation energies have only been observed for the reactions of CuO-Cu_2O and Cu_2O-Cu, where we indeed observed a negligible temperature effect. The activation energies of around 3 kJ/mol are not caused by intraparticle mass transfer limitations, since we have proven before that mass transfer limitations do not play a role (see also [17,18]). A reason that we find plausible is that the oxygen diffusion does not occur via molecular oxygen, as it has been already indicated in a previous work [26], but via oxygen vacancies, where a double-effect could be observed between the formation of lattice oxygen and electron transfer, resulting in an almost zero activation energy.

The external mass transfer towards the particles and the internal diffusion in the oxygen carrier particles is described with the Maxwell-Stefan equations [33] based on the following assumptions:

- The particle is porous, spherical and symmetrical.
- The volume of the particle is constant.
- The structure of the particle is uniform and can be represented by a porosity, tortuosity and average pore size and the system is isobaric.

The model consists of a set of particle differential equations, viz. the mass balances of gaseous and solid components and the energy balance. To solve the system of PDE's, a technique using grid refinement near the external surface of the particle and time-step adaptation is used [33]. The typical grid sizes for the radial direction (particle) were in the order of 100 points and the time step was in the order of 0.1–1 ms (See Section 3.1). For further details, the reader is referred to our previous work [27].

In this model, the generalized Fick equations are used for the calculation of the diffusive mass fluxes n_i, [34], considering both the effects of diffusion and drift fluxes.

The governing equations for the particle model and the associated initial and boundary conditions are summarized in Tables 4 and 5.

Typically three solid components (Me, MeO and an inert component) are present in CLC systems. For the case of only three solid components, only one solid balance needs to be considered, as the weight fraction of the other components follows from the conservation of the number of moles of solid and the conservation of mass of the inert material. In this work, for CuO/Al_2O_3, the CuO reacts with the support. Therefore, there are more MeO and Me species. Each reduction reaction was considered as an independent oxygen carrier system with also three components (MeO, Me and inert). Therefore, for each reduction reaction, the mass balance was following also the conservation of the number of moles of solid and the conservation of mass of the inert material.

It is necessary to properly calculate the local porosity, the mass and the conversion of the particle and it is also necessary to estimate the

Table 3
Summary of the reaction rate constants used to describe the redox kinetics.

Reactions	Reaction rate expression	Pre-exponential factor	Activation Energy (kJ/mol)
Reduction			
Tenorite reduction $k_{red,1}$ ($s^{-1}bar^{-1}$)	$r_{red,1} = k_{red,1}C_{CuO}P_{H_2}$	$1.63{\cdot}10^{-1}$	0.15
Cuprite reduction $k_{red,2}$ ($s^{-1}bar^{-1}$)	$r_{red,2} = k_{red,2}C_{Cu_2O}P_{H_2}$	$1.61{\cdot}10^{-2}$	1.79
First spinel reduction, r_{sp1} ($s^{-1}bar^{-1/2}$)	$r_{sp1} = k_{sp1}C_{CuAl_2O_4}P_{H_2}$	$3.87{\cdot}10^{10}$	241.75
Second spinel reduction, r_{sp2} ($s^{-1}bar^{-1/2}$)	$r_{sp2} = k_{sp2}C_{CuAl_2O_4}P_{H_2}$	1.09	0.37
Third spinel reduction, r_{sp3} ($s^{-1}bar^{-1/2}$)	$r_{sp3} = k_{sp3}C_{CuAlO_2}P_{H_2}$	$9.75{\cdot}10^{-03}$	8.85
Oxidation			
First oxidation reaction, r_{ox1} ($s^{-1}bar^{-1/2}$)	$r_{ox1} = k_{ox1}C_{Cu}P_{O_2}^{1/2}$	$8.54{\cdot}10^{-01}$	0.83
Second oxidation reaction, r_{ox2} (s^{-1})	$r_{ox2} = k_{ox2}C_{CuO}C_{Al_2O_3}$	$1.27{\cdot}10^{-06}$	1.18
Third oxidation reaction, r_{ox3} (s^{-1} $bar^{-1/2}$)	$r_{ox3} = k_{ox3}C_{CuAlO_2}C_{Al_2O_3}P_{O_2}^{1/2}$	$1.98{\cdot}10^{-05}$	0.71

Table 4
Governing equations in the particle model.

Continuity equation	$\frac{\partial(\varepsilon_g \rho_g)}{\partial t} = \frac{1}{r^2}\frac{\partial(r^2 n_{tot})}{\partial r} + \sum_{i=1}^{N_g} \nu_i r_i M_i$
Gas phase components	$\frac{\partial(\varepsilon_g \rho_g \omega_{g,i})}{\partial t} = \frac{1}{r^2}\frac{\partial(r^2 n_i)}{\partial r} + \nu_i r_i M_i$
where	$n_i = j_i + \omega_{g,i} n_{tot} = -\rho_g \sum_{k=1}^{N_g-1} (d_{eff,i,k}\frac{\partial \omega_{g,k}}{\partial r}) + \omega_{g,i} n_{tot}$
Solid phase components	$\frac{\partial(\varepsilon_s \rho_s \omega_{s,j})}{\partial t} = \sum_{k=1}^{N_R} \nu_{k,j} r_k M_j$
where	$\omega_{s,MeO} = \omega_{s,act}^{ox}(1-\omega_{s,Me}) - \omega_{s,Me}(1-\omega_{s,act}^{ox})\frac{\nu_s M_{MeO}}{M_{Me}}$
Energy balance	$(\varepsilon_g \rho_g C_{p,g} + \varepsilon_s \rho_s C_{p,s})\frac{\partial T}{\partial t} = \frac{1}{r^2}\frac{\partial}{\partial r}(r^2 \lambda_{eff}\frac{\partial T}{\partial t}) - \sum_{i=1}^{N_R}(-r_i \Delta H_{R,i})$

physical properties of the solid material, therefore it is important to keep track of the local composition of solid components in the particle. To achieve this, pure species data (including the spinel compounds) obtained from Ihsan Barin [35] and García-Labiano et al. [36] were used. For the gaseous components, physical properties were obtained from the data sheets of Daubert and Danner [37].

To calculate the amount of tenorite- and cuprite spinel in the oxygen carrier at the start of a reduction cycle, a quantification has been carried out based on the results obtained from TGA measurements, as has been done in a previous work [18]. Comparing the tenorite and cuprite spinel concentrations at the end of the reduction and using the fact that the initial concentration of $CuAl_2O_4$ is 6 wt%, the concentrations of $CuAl_2O_4$ and $CuAlO_2$ have been calculated and they are summarized in Table 6. The final amounts after the reduction reaction are the initial amounts for the oxidation reactions.

Diffusive transport of gas phase components inside the particle is described with the Maxwell-Stefan diffusivities d_{eff}, while mass and energy transport between the bulk gas phase and the catalyst surface is calculated with the mass transfer coefficients obtained with the method of Toor, Stewart and Prober. For more details the reader is referred to Tiemersma et al. [38].

The particle model was used to obtain particle effectiveness factors, η, for all the gas-solid reactions as a function of the particle conversion. The particle effectiveness factor changes with the increasing particle conversion because the process is inherently transient and the reaction rate changes with time. The solids conversion is defined as follows:

$$X = \frac{w_{s,in} - w_s}{w_{s,in}} \quad (1)$$

where $w_{s,in}$ denotes the initial mass fraction of the solid reactant and w_s the mass fraction at a certain moment during the reduction cycle.

The correlations developed with the particle model with the embedded grain model for the effectiveness factor for each reduction reaction are summarized in Table 7 for the 5 mm particle size that have been included in the reactor model for the large scale simulations (see Section 4.3).

The effectiveness factor for the gas-solid reactions is clearly decreasing with particle conversion as the availability of the reacting solid phase is also decreasing as a function of conversion. This is indeed also visible in Fig. 1 where the effectiveness factor for the tenorite reduction is plotted as a function of the particle conversion, as an example. The same figure also reports the intra-particle radial concentration profiles of tenorite at two different particle conversions. As is clear from the figure, when the solids conversion increases, the reactive solids concentration decreases and the effectiveness factor decreases. These effectiveness factors are thus a correction factor for the radial concentration profiles of in particular the solids phases inside the particle.

Table 6
Initial solid compositions at the start of the reduction cycles.

Temperature	$CuAl_2O_4$ (wt%)	$CuAlO_2$ (wt%)
600 °C	1.5	4.5
800 °C	1.433	1.567
1000 °C	0.183	0.317

Table 7
Effectiveness factor correlations as a function of the particle conversion.

Reactions	5 mm
Tenorite reduction	$0.169X^2 - 0.3719X + 0.2075$
Cuprite reduction	$-0.1761X^3 + 0.3984X^2 - 0.3128X + 0.0906$
First spinel reduction	$-0.1758X^3 + 0.3497X^2 - 0.2204X + 0.0455$
Second spinel reduction	$-0.2858X + 0.285$
Third spinel reduction	1

4. Results and discussion

In this section first a validation of the reactor model with experimental results is carried out using the 'stop and check' experiments and breakthrough experiments in the lab-scale PBR setup (Section 4.1). Subsequently, in Section 4.2, the importance of accounting for the formation and reduction of spinel compounds in the lab-scale packed bed reactor is investigated and discussed. Finally, Section 4.3 addresses the importance of spinel formation to assess the reactor performance of a large industrial-scale packed bed reactor.

Before showing and discussing the experimental results, the absence of internal mass transfer limitations in the lab-scale reactor was first assured with a redox experiment that was carried out with oxygen carrier particles of 1.1 mm diameter and with crushed particles (with the particle size in the range of 1–574 μm, measured with a Fritsch Analysette 22). In Fig. S.4 from the Supplementary Material, the hydrogen breakthrough curves have been compared for a reduction cycle at 1000 °C, from which it can be concluded that internal mass transfer limitations indeed do not play a role for oxygen carrier particles of 1.1 mm diameter, as was expected on the basis of earlier TGA experiments [18,39]. It is important to note that the absence of internal mass transfer limitations only holds for the lab-scale reactor with relatively

Table 5
Initial and boundary conditions for the particle model.

Condition	Component balance (gas phase)	Energy balance
t = 0	$\omega_{g,N_2} = 1.0$	$T = T_{bulk}$
r = 0 (center)	$\left.\frac{\partial \omega_{g,i}}{\partial r}\right\|_{r=0} = 0$	$\left.\frac{\partial T}{\partial r}\right\|_{r=0} = 0$
r = R (surface)	$-\sum_{k=1}^{N_g-1} d_{eff,i,k}\frac{\partial \omega_{jk}}{\partial r} = \sum_{k=1}^{N_g-1} k_{g,ik}(\omega_{g,k} - \omega_{bulk,k})$	$\lambda_{eff}\frac{\partial T}{\partial r} = \alpha(T - T_{bulk})$
	Film model $k_{g,ik} = \Xi_{i,k} k_{g,ik}^0$ where $\Xi_{i,k} = \frac{\Phi_{ik}}{\exp(\Phi_{ik}) - 1}$ and $\Phi_{ik} = \frac{n_{tot}}{\rho_g k_{g,ik}^0}$	

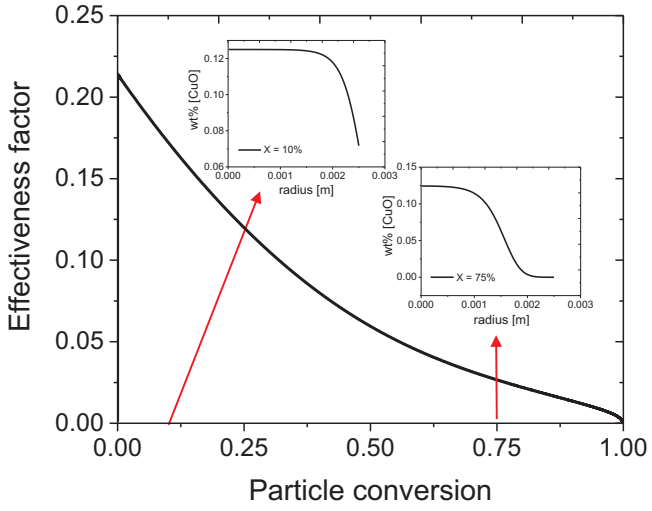

Fig. 1. Effectiveness factor as a function of the particle conversion for the tenorite reduction; Concentration of CuO as a function of the radial position for two different particle conversion.

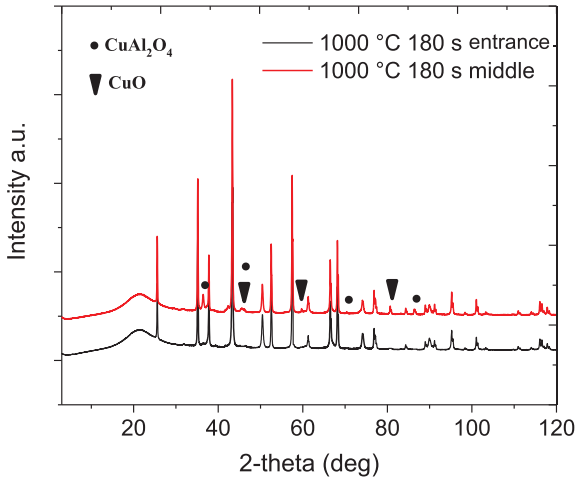

Fig. 3. XRD patterns for samples taken from the entrance and the middle of the reactor stopping the reduction after 180 s, at 1000 °C with 10% H_2–90% N_2.

small oxygen carrier particles. For large industrial-scale reactors with bigger oxygen carrier particles, internal mass transfer limitations will become important and need to be taken into account as will be shown and discussed in Section 4.3.

4.1. Validation of the reactor model with experimental results

4.1.1. Stop and check experiments

Experiments were carried out in a lab-scale PBR setup at 1000 °C stopping the reduction at two different reduction times, viz. $t_1 = 180$ s (the bed is not fully reduced on the basis of the breakthrough experiments shown in Fig. S.4), and $t_2 = 500$ s (the bed is almost fully reduced according to the results in Fig. S.4) and taking samples of the oxygen carrier from the entrance and the middle of the reactor, which were analyzed with XRD and the results were compared with model simulation results.

4.2. Reduction time of 180 s

In Fig. 2a, the concentration of the spinel compounds $CuAl_2O_4$ and $CuAlO_2$ calculated with the model are plotted as a function of the axial position in the bed for a reduction time of 180 s. Fig. 2b shows the axial concentration profile of copper at the same time, showing that the bed is indeed only partially reduced. The simulations show that almost all the $CuAl_2O_4$ is reduced to Cu and that only a very minor amount of $CuAlO_2$ is present in the oxygen carrier (Fig. 2a). At the entrance of the reactor, most of the $CuAlO_2$ has been further reduced to Cu, while at the beginning of the reaction front the $CuAlO_2$ concentration is maximal, but still below 0.15 wt%.

A difference in color was observed for the particles extracted from the two different positions in the reactor indicating a different composition. In Fig. 3, the XRD patterns for the two samples are given. In both samples the phases Al_2O_3, Cu and $CuAlO_2$ (not marked in the XRD pattern) were observed. In the sample taken from the middle of the reactor (red line), also CuO and $CuAl_2O_4$ were found, as expected from the simulations. Note that only the representative peaks are marked in Fig. 3.

4.3. Reduction time of 500 s

The axial concentration profiles of $CuAl_2O_4$, $CuAlO_2$ and Cu calculated with the model for a reduction time of 500 s at 1000 °C are shown in Fig. 4, showing that the bed is almost fully reduced to Cu, that $CuAl_2O_4$ is no longer present and that only a very small amount of $CuAlO_2$ remains, as was expected on the basis of previous experimental work [18].

Particles from the entrance and from the middle of the reactor were extracted and further analyzed with XRD. The XRD patterns shown in Fig. 5 of the two samples are identical and only the presence of Cu, Al_2O_3 and a small amount of $CuAlO_2$ (not marked) is observed, corresponding to the simulation results.

In the next sections the model will be validated in more detail comparing the computed and experimentally determined breakthrough curves for both the reduction and oxidation cycles.

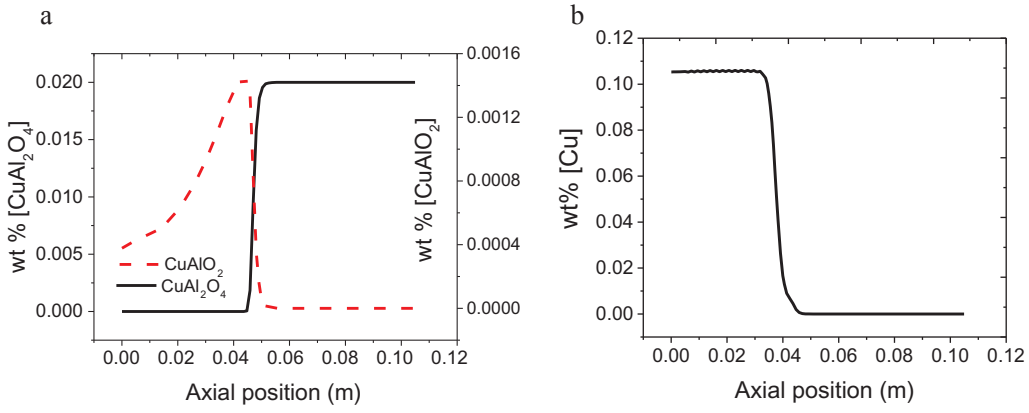

Fig. 2. Stop and check experiments stopping the reduction after 180 s, at 1000 °C with 10% H_2–90% N_2 for (a) $CuAl_2O_4$ and $CuAlO_2$ spinel, (b) copper.

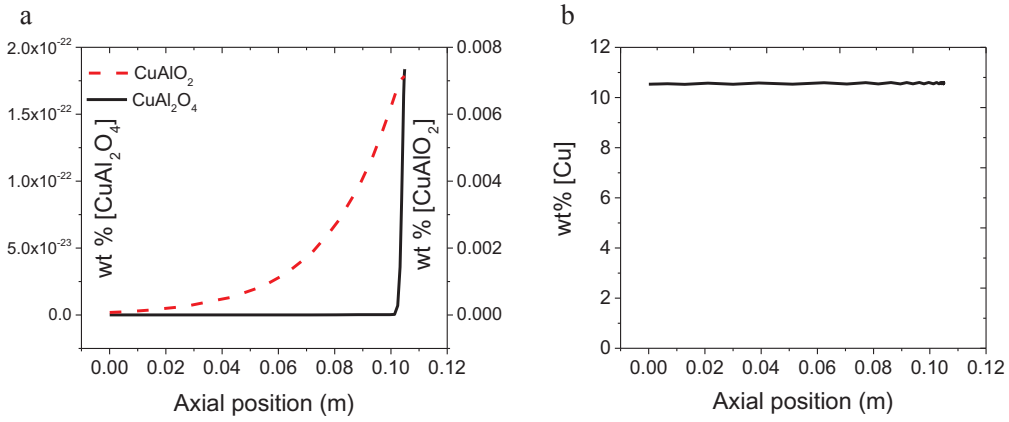

Fig. 4. Stop and check experiments stopping the reduction after 500 s, at 1000 °C with 10% H_2–90% N_2 for (a) $CuAl_2O_4$ and $CuAlO_2$ spinel, (b) copper.

4.3.1. Breakthrough curves validation

The hydrogen and oxygen breakthrough curves from the reduction and oxidation cycle respectively, as computed by the model and obtained experimentally in the lab-scale set-up, have been compared for redox cycles carried out at two different temperatures, viz. 1000 °C and 600 °C, shown in Figs. 6 and S.5 from the Supplementary Material, respectively. In these figures the simulation results of the reactor model with the effectiveness factors derived with the detailed particle model are referred to as 'simulation SP', referring to the fact that the formation of spinel compounds is fully accounted for, whereas 'SCM' refers to the results for the reduction cycle from a reactor model where the gas-solid kinetics has been simplified with a shrinking model [26] only considering the CuO reduction to Cu and ignoring the formation and reaction of spinel compounds.

To assure that the slow-down in the reaction rate observed when comparing the reactor model simulations with the effectiveness factors from the particle model with the detailed kinetics (simulation SP) and the SCM (Fig. 6) is not caused by dispersion but is related to the gas-solid kinetics, a comparison of the breakthrough curves between the simulations that do and do not account for axial dispersion in the reactor has been carried out (see Fig. S.6 of Supplementary Material). The results clearly demonstrate that there is no influence of mass dispersion, as was already expected from Fig. S.4, because the extent of dispersion is a function of the particle diameter and it was shown that the particle size does not influence the breakthrough curves.

Overall, Figs. 6 and S.5 of the Supplementary Material show a quite reasonable agreement between the experimental results and the simulations carried out with the effectiveness factors developed with the particle model with the detailed gas-solid kinetics, for both the breakthrough times as well as how the H_2 and O_2 is consumed in the reactor during the reduction and oxidation cycles at different temperatures.

In addition, Fig. 6a shows that a simple SCM that only considers CuO reduction to Cu is unable to describe the breakthrough curves. In particular, the breakthrough curve for the SCM is much steeper and the increase in the hydrogen concentration at the outlet starts at a much later moment in time (at ca. 450 s), because in this model all the CuO is reduced directly to Cu without any restrictions. For the SP simulations the outlet hydrogen concentration starts to increase much earlier (around 390 s), because not all the spinel ($CuAl_2O_4$ and $CuAlO_2$) has been converted to Cu yet.

This is further corroborated in Fig. 7a, that shows that the total amount of Cu after 300 s of reduction for the SP simulations is indeed smaller than for the model with the SCM, because not all the spinel has been reduced to Cu, resulting in a smaller hydrogen breakthrough time for the SCM compared to the SP model (see Fig. 7b). However, for the SP model the hydrogen already starts to slip well before all the CuO and spinel compounds have been fully reduced to Cu, which is also evident from the much more dispersed axial concentration profiles of Cu and H_2. Thus, the formation of the spinel compounds and kinetic limitations in their reduction cause a much more dispersed reaction front and may limit the final conversion of Cu.

Fig. 8 provides the axial concentration profiles of the spinel compounds at different moments during the reduction computed with the SP model, clearly showing that indeed all the $CuAl_2O_4$ gets fully reduced when the reaction front progresses, while for the same reduction time, there is still some amount of $CuAlO_2$ present. The kinetic limitations in the reduction of $CuAlO_2$ to Cu explain the differences in the final amount of Cu between the SP and SCM simulations (Fig. 7a).

Having a closer look at Figs. 6 and S.5 from the Supplementary Material, respectively, it can be concluded that the model has a good agreement with the experiments, but there is a small deviation in the last part of the breakthrough curve, where the model over predicts somewhat the reduction rate compared to the experimental results. Apparently the reduction rate of the tenorite spinel $CuAlO_2$ is somewhat overestimated (see Fig. 8).

4.4. Importance of spinel compounds for a lab-scale packed bed reactor

The importance of accounting for the formation and reduction of spinel compounds in the particle model is further investigated for the lab-scale packed bed reactor, where the hydrogen breakthrough curve of a reduction experiment at 600 °C is compared with the numerical results from two different simulations, where one fully accounts for the reduction of spinel compounds (indicated with SP), whereas the other assumes infinitely fast spinel reduction kinetics (indicated with 'Fast spinel') and thus assumes full conversion of CuO to Cu without accounting for kinetic limitations of the spinel compounds (see Fig. 9).

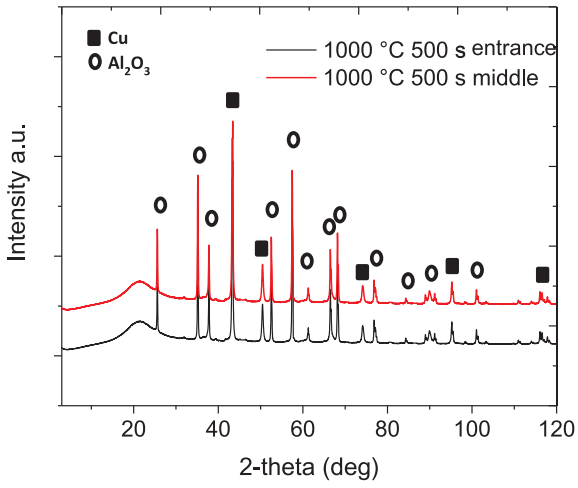

Fig. 5. XRD patterns for particles taken from the entrance and the middle of the reactor stopping the reduction after 500 s, at 1000 °C with 10% H_2–90% N_2.

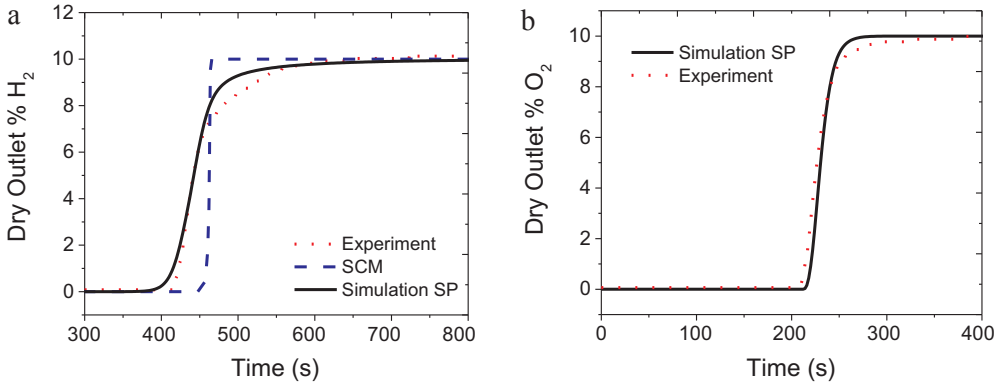

Fig. 6. Comparison between the simulation and the experiment for the breakthrough curves during redox cycles at 1000 °C for (a) reduction with 10% H_2–90% N_2; (b) oxidation with 10% O_2–90% N_2. ('Simulation SP' refers to the reactor model fully accounting for the formation and reaction of spinel compounds, whereas 'SCM' refers to the shrinking core model).

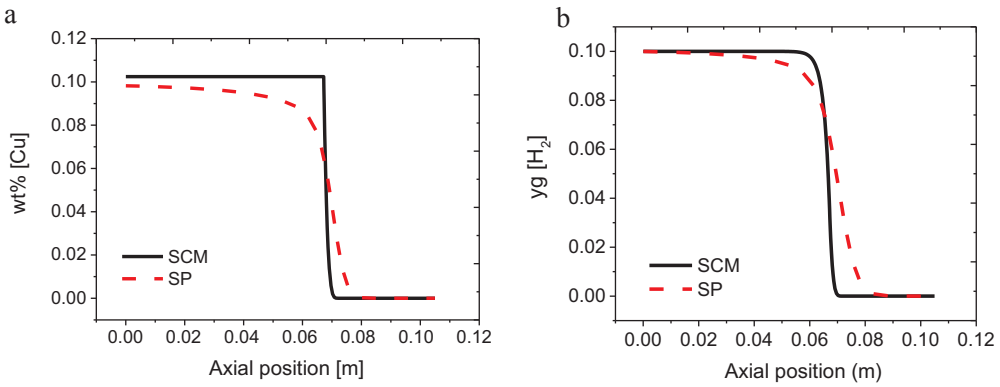

Fig. 7. Comparison of the axial concentration profiles from the SP and SCM simulations after 300 s of reduction at 1000 °C for: (a) Cu, (b) H_2.

For the SP simulation the hydrogen starts to break through considerably faster than for the simulation with the infinitely fast spinel reduction kinetics, respectively 404 and 420 s. This can be attributed to the fact that at 600 °C $CuAl_2O_4$ is only reduced to $CuAlO_2$, and $CuAlO_2$ is not further reduced to Cu, because this reaction is only favored at higher temperatures. Thus, the amount of hydrogen that reacts with the oxygen carrier is smaller in the SP simulation, resulting in a smaller breakthrough time.

In Fig. 10, the computed axial concentration profiles of Cu, H_2 and both spinel species ($CuAl_2O_4$ and $CuAlO_2$) are shown for both models (SP and Fast spinel) after 300 s of reduction at 600 °C. It can be observed that the amount of Cu is lower in the model that accounts for the kinetic limitations of the spinel species (SP), because the formed $CuAlO_2$ is hardly reduced to Cu at this temperature, whereas the $CuAl_2O_4$ is fully converted.

In this section, for both, experimental and modelling, particles of 1.1 mm diameter CuO/Al_2O_3 have been used, because of their availability. Although it is well-know, that for practical scale-up packed bed reactors, much bigger particle sizes need to be used, as it is present in the next section.

On the basis of the discussed results it can be concluded that it is important to account for the formation and reduction of spinel compounds to accurately calculate the width of the reaction front and the breakthrough time, as well as the amount of Cu in the bed after the reduction cycle. Part of the spinel species does not react in the reaction front but later, which also influences the axial temperature profiles in the bed and the temperature rise that can be achieved in the packed bed chemical looping combustion reactor. This effect is larger and important for large-scale packed bed reactors, which will be further investigated in the next section.

4.5. Importance of spinel formation for an industrial scale packed bed reactor

The importance of an accurate description of the gas-solid kinetics of the CuO/Al_2O_3 oxygen carrier has been further investigated with the model for an industrial scale packed bed reactor (see Table 8), where the paper by Spallina et al. [40] has been used as reference for the

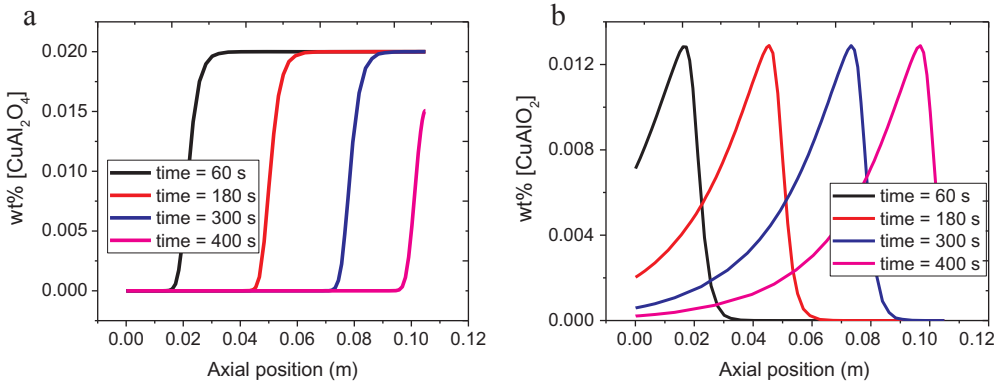

Fig. 8. Axial concentration profiles of the spinel compounds calculated with the SP model for different moments in time during the reduction at 1000 °C with a 10% H_2–90% N_2 mixture for (a) $CuAl_2O_4$, (b) $CuAlO_2$.

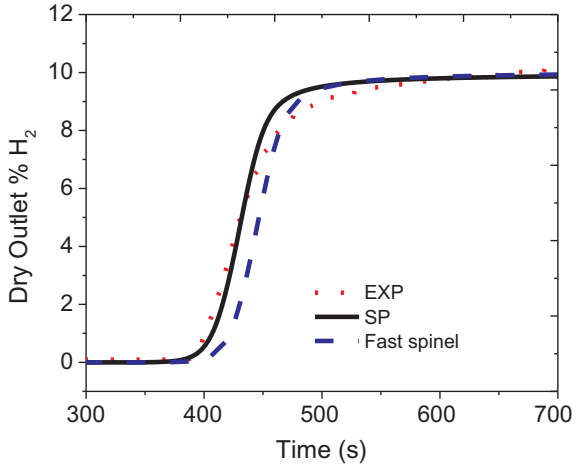

Fig. 9. Comparison of the hydrogen breakthrough curves obtained from a simulation fully accounting for the spinel compounds (SP), a simulation assuming infinitely fast reduction kinetics of the spinel compounds (Fast spinel) and the experiment for a reduction at 600 °C with 10% H_2–90% N_2.

reactor dimensions. Although the oxygen carrier and the reducing gases are different from the ones used in this work, the parameters obtained by Spallina provide a good approximation.

For this industrial scale reactor, larger particles of 5 mm diameter need to be applied because of pressure drop considerations. To study whether internal mass transfer limitations need to be taken into account for this particle size and the possible effect thereof, different simulations have been carried out for different particle diameters with and without accounting for internal mass transfer limitations, indicated with 'MT' and 'NO MT' respectively (see Fig. 11).

The figure clearly shows that for particles of 1.1 mm diameter (as used in the experiments of the lab-scale reactor), mass transfer limitations are unimportant, however, for particles larger than 2 mm mass transfer limitations start to become prominent, and it is necessary to account for internal mass transfer limitations to correctly describe the breakthrough time and the dispersion of the reaction front (more simulations for different particle sizes are provided in Fig. S.7 of the Supplementary Material).

Table 8
Parameters used in the large-scale packed-bed reactor simulations.

Reactor	
Length, m	11
Diameter, m	5.5
Wall Temperature, K	873
Oxygen Carrier	
Particle diameter, mm	5
CuO content, %wt	12.5
Packed Bed density, kg/m^3	1330
Reduction	
Total mass flow rate, kg/s	60
Pressure, bar	17
Temperature, K	873
Composition, %vol	60 N_2; 40 H_2

In Fig. 12, the intra-particle concentration profiles are plotted for the reduction with a 10% H_2-90% N_2 gas mixture at 1000 °C for particles of 1.1 mm and 5 mm diameter.

Fig. 12a shows that for the particles of 5 mm diameter, the radial concentration profiles of both $CuAl_2O_4$ and CuO are very steep for different degrees of particle conversion, indicating that mass transfer limitations play an important role, while Fig. 12b, for the particles of 1.1 mm diameter, the profiles of CuO are much flatter, indicating that mass transfer limitations are much less pronounced. Nevertheless, the spinel concentration profile for the 1.1 mm particle still shows a considerable gradient, which is caused by the extremely fast tenorite spinel reduction kinetics at 1000 °C.

In order to show the importance of including spinel kinetics for the reduction step of CLC in an industrial-scale packed bed reactor, again simulations with two different models were performed, one with the reactor model with the effectiveness factors from the particle model

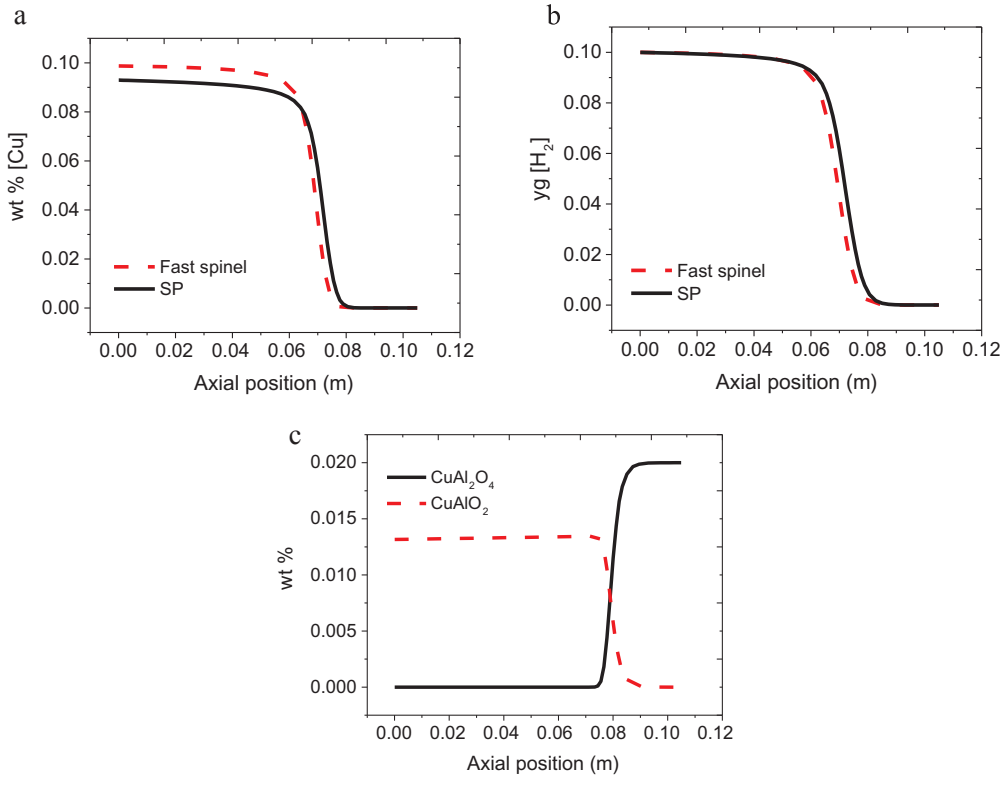

Fig. 10. Axial concentration profiles computed by the model that fully accounts for the kinetic limitations of the spinel compounds (SP) and the model that assumes infinitely fast spinel reaction kinetics (Fast spinel) after 300 s of reduction at 600 °C with a 10% H_2–90% N_2 gas mixture for (a) Cu, (b) H_2, (c) $CuAl_2O_4$ and $CuAlO_2$ (only SP).

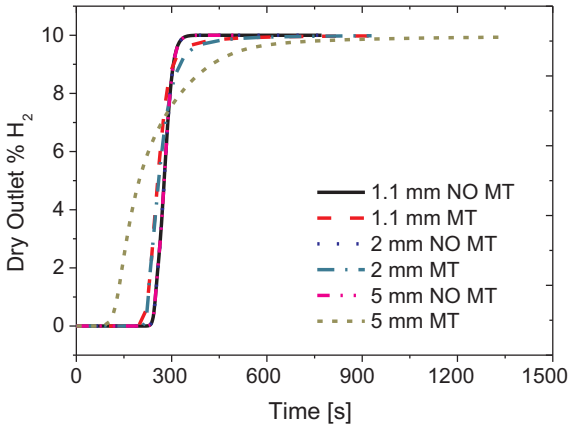

Fig. 11. Breakthrough curves calculated with the SP model with and without accounting for internal mass transfer limitations (MT and NO MT) for different particle diameters of 1, 2 and 5 mm.

that fully accounts for the spinel species (SP) and the model that assumes infinitely fast spinel reduction kinetics (Fast spinel). In Fig. 13 the hydrogen breakthrough curves computed by both models are shown. Fig. S.8 of the Supplementary Material shows the axial Cu concentration profiles at different moments in time during the reduction with a 10% H_2-90% N_2 mixture at 600 °C and 1000 °C. For the reduction at 600 °C, there is a large difference in the breakthrough curves for the two models, 300 s for SP vs. 312 s for the Fast spinel model, again caused by the kinetic limitations of $CuAlO_2$ to Cu at 600 °C for the SP model. For the reduction at 1000 °C the differences are smaller (308 s for the SP simulation vs. 312 s for the Fast spinel model), because at this temperature all the $CuAl_2O_4$ and a large part of the $CuAlO_2$ have been reduced to Cu, as evident from Fig. S.8. Figs. S.9 and S.10 of the Supplementary Material show the calculated axial concentration profiles of CuO, Cu, $CuAl_2O_4$ and $CuAlO_2$ for a reduction time of 240 s at 600 °C and 1000 °C respectively. As discussed before, all the $CuAl_2O_4$ is reduced at both temperatures, but not all the $CuAlO_2$ gets reduced, where at 600 °C its reduction is negligible, but at 1000 °C considerable, but not complete.

Due to the slow $CuAlO_2$ reduction kinetics, the final amount of Cu in the bed is smaller for the SP simulations than for the simulation that assumes infinitely fast spinel kinetics where all the spinel is converted to Cu. However, for the reduction at 1000 °C the difference is very small because the $CuAl_2O_4$ is mostly converted to Cu and there is only a very small amount of $CuAlO_2$ unconverted to Cu (see Fig. S.10).

The differences in the conversion to Cu also affects the axial temperature profiles. The axial temperature profiles for the SP and Fast spinel simulations are shown in Fig. 14 for the two considered reduction temperatures, viz. 600 °C and 1000 °C, where the total initial amount of CuO and $CuAl_2O_4$ was the same. The maximum temperature reached in with the model fully accounting for the spinel kinetics is smaller than the maximum temperature with the model that assumes infinitely fast spinel reduction kinetics, about 20 °C. At the conditions present in the bed, the active component of the oxygen carrier does not fully react, i.e. the $CuAlO_2$ is not fully converted, and as a consequence the heat released in the SP simulation is smaller than for the Fast spinel model, where all the components are reduced to Cu.

All these differences indicate the importance of using an accurate particle model that fully accounts for the formation and reduction of spinel compounds to adequately predict the breakthrough time (and thus possible fuel slip), the final amount of Cu in the bed at the end of the reduction cycle, and thus the temperature rise and reactor performance of packed-bed chemical looping reactors employing a CuO/Al_2O_3 oxygen carrier.

5. Conclusions

A one-dimensional, pseudo-homogeneous packed-bed reactor model with effectiveness factors for the gas-solid reactions developed with a detailed particle model embedding a pseudo-homogeneous grain model was developed and validated with experiments carried out in a lab-scale packed-bed reactor setup for chemical looping combustion using CuO/Al_2O_3 as oxygen carrier. Stop and check experiments have confirmed the presence of different forms of spinel during the reduction reactions, which the developed model was able to describe adequately, when fully

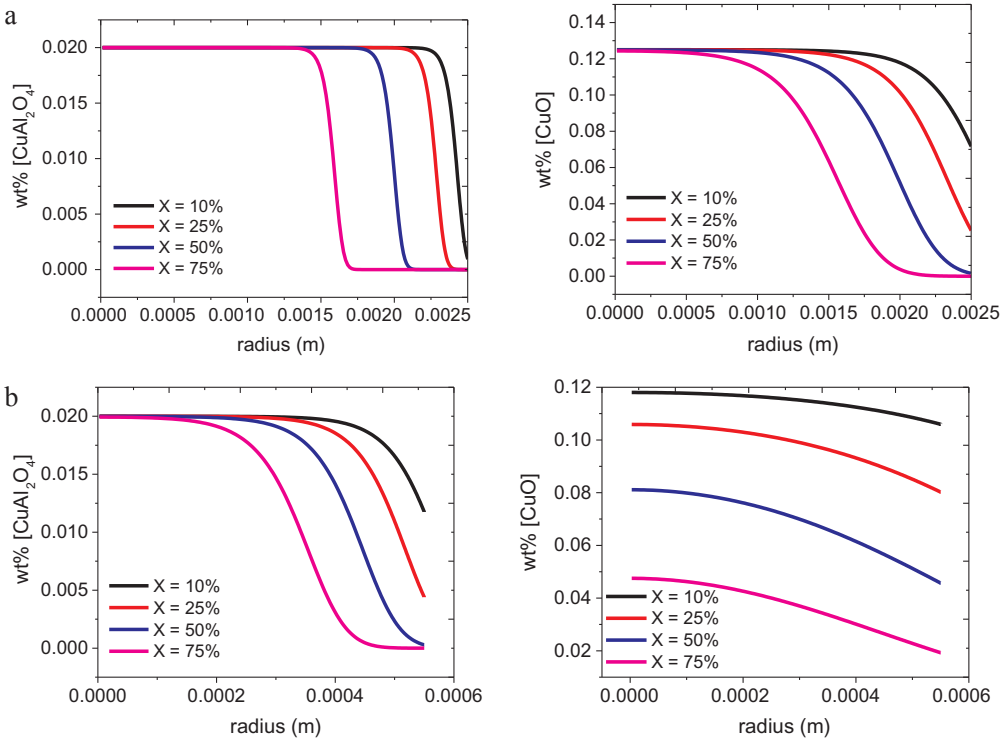

Fig. 12. Intra-particle concentration profiles of $CuAl_2O_4$ and CuO during the reduction at 1000 °C with a 10% H_2–90% N_2 gas mixture for: (a) 5 mm diameter particle, (b) 1.1 mm diameter particle.

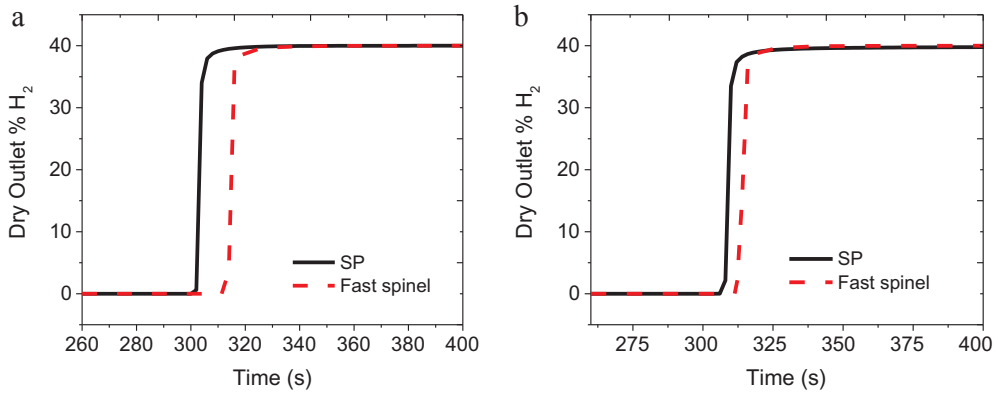

Fig. 13. Comparison of the computed hydrogen breakthrough curves for the model that fully accounts for the spinel kinetics (SP) and the model that assumes infinitely fast spinel reduction kinetics for a reduction with a 10% H_2–90% N_2 mixture at (a) 600 °C, (b) 1000 °C.

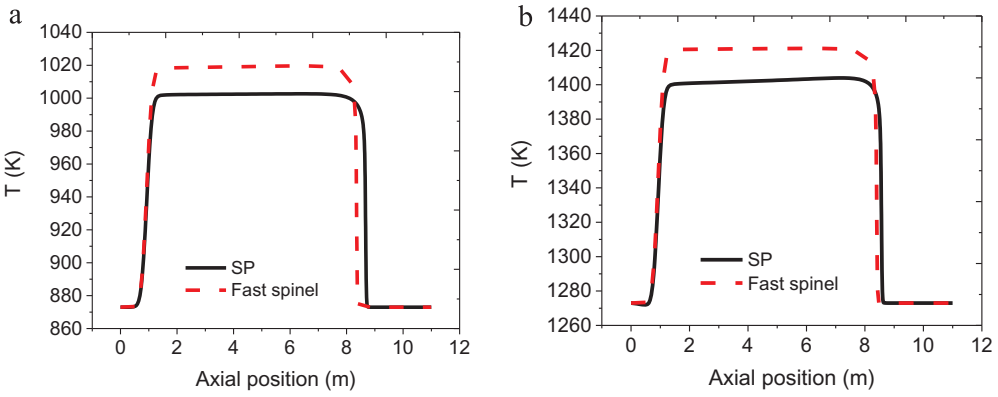

Fig. 14. Axial temperature profiles for the SP and Fast spinel simulations after 240 s of reduction with a 10% H_2–90% N_2 mixture at: (a) 600 °C and (b) 1000 °C.

accounting for the kinetics of the formation and reduction of the spinel compounds. The importance of accurate gas-solid kinetics including the spinel compounds was demonstrated by comparison with a conventional simplified SCM ignoring spinel compounds, where the simulations with the SCM resulted in a mismatch of the predicted breakthrough time and the amount of Cu present in the bed after the reduction, whereas the model that fully accounts for the spinel kinetics quite adequately describes the breakthrough curves measured in the lab-scale packed-bed reactor. Moreover, by comparing simulation results from the model that fully accounts for the formation and reduction kinetics of the spinel compounds with a model that assumes infinitely fast spinel reduction kinetics it was concluded that an accurate description of the gas-solid kinetics is required to accurately describe the dispersion of the reaction front (hence the fuel slip), the breakthrough time and the amount of Cu present in the bed after the reduction cycle, especially due to the slow reduction kinetics of $CuAlO_2$. Finally, it was shown with simulations for a large-scale packed bed reactor that kinetic limitations of the spinel reduction also reduces the maximum temperature rise (about 20 °C) that can be achieved in the packed bed during chemical looping combustion, which has to be compensated for by an increase in the Cu-content of the oxygen carrier. This confirms that it is necessary to include particle effectiveness factors for gas-solid reactions developed with a detailed particle model that accounts for all the reduction mechanisms occurring in the CuO/Al_2O_3 oxygen carrier, including the spinel compounds.

Acknowledgements

The research leading to these results has received financial support from Netherlands Organisation for Scientific Research (NWO) through the ECHO-STIP project.

Appendix A. Supplementary data

Supplementary data associated with this article can be found, in the online version, at http://dx.doi.org/10.1016/j.cej.2017.11.138.

References

[1] M.M. Hossain, H.I. de Lasa, Chemical-looping combustion (CLC) for inherent CO2 separations-a review, Chem. Eng. Sci. 63 (2008) 4433–4451, http://dx.doi.org/10.1016/j.ces.2008.05.028.
[2] A. Lyngfelt, Chemical-looping combustion of solid fuels – status of development, Appl. Energy 113 (2013) 1869–1873.
[3] J. Wolf, M. Anheden, J. Yan, Comparison of nickel- and iron-based oxygen carriers in chemical looping combustion for CO2 capture in power generation, Fuel 84 (2005) 993–1006.
[4] S. Noorman, M. van Sint Annaland, Packed bed reactor technology for chemical-looping combustion, Ind. Eng. Chem. Res. 46 (2007) 4212–4220, http://dx.doi.org/10.1021/ie061178i.
[5] V. Spallina, M.C. Romano, P. Chiesa, F. Gallucci, M. Van Sint Annaland, G. Lozza, Integration of coal gasification and packed bed CLC for high efficiency and near-zero emission power generation, Int. J. Greenhouse Gas Control 27 (2014) 28–41.
[6] B. Kronberger, E. Johansson, G. Löffer, T. Mattisson, A. Lyngfelt, H. Hofbauer, A two-compartment fluidized bed reactor for CO2 capture by chemical-looping combustion, Chem. Eng. Technol. 27 (2004) 1318–1326.
[7] A. Lyngfelt, B. Leckner, T. Mattisson, A fluidized-bed combustion process with inherent CO2 separation; application of chemical-looping combustion, Chem. Eng. Sci. 56 (2001) 3101–3113.
[8] T. Proll, P. Kolbitsch, H. Hofbauer, A novel dual circulating fluidized bed system for chemical looping processes, IFAC Proc. 7 (2009) 405–410, http://dx.doi.org/10.1002/aic.
[9] S. Jiang, L. Shen, J. Wu, J. Yan, T. Song, The investigations of hematite-CuO oxygen carrier in chemical looping combustion, Chem. Eng. J. 317 (2017) 132–142, http://dx.doi.org/10.1016/j.cej.2017.01.091.
[10] X. Wang, Z. Chen, M. Hu, Y. Tian, X. Jin, S. Ma, et al., Chemical looping combustion of biomass using metal ferrites as oxygen carriers, Chem. Eng. J. 312 (2017) 252–262, http://dx.doi.org/10.1016/j.cej.2016.11.143.
[11] C. Lin, W. Qin, C. Dong, Reduction effect of α -Fe 2 O 3 on carbon deposition and CO oxidation during chemical-looping combustion, Chem. Eng. J. 301 (2016) 257–265, http://dx.doi.org/10.1016/j.cej.2016.04.136.
[12] H.P. Hamers, F. Gallucci, G. Williams, M. van Sint Annaland, Experimental demonstration of CLC and the pressure effect in packed bed reactors using NiO/CaAl2O4 as oxygen carrier, Fuel 159 (2015) 828–836, http://dx.doi.org/10.1016/j.

fuel. 2015.07.034.
[13] M. Ortiz, F. Gallucci, F. Snijkers, J. Van Noyen, E. Louradour, D. Tournigant, et al., Development and testing of ilmenite granules for packed bed chemical-looping combustion, Chem. Eng. J. 245 (2014) 228–240, http://dx.doi.org/10.1016/j.cej.2014.02.030.
[14] V. Spallina, M.C. Romano, P. Chiesa, F. Gallucci, M. van Sint Annaland, G. Lozza, Integration of coal gasification and packed bed CLC for high efficiency and near-zero emission power generation, Int. J. Greenhouse Gas Control 27 (2014), http://dx.doi.org/10.1016/j.ijggc.2014.04.029.
[15] P. Hamers, F. Gallucci, M. Van Sint Annaland, A novel reactor configuration for packed bed chemical-looping combustion of syngas, Int. J. Greenhouse Gas Control (2013).
[16] H.P. Hamers, M.C. Romano, V. Spallina, P. Chiesa, F. Gallucci, M. van Sint Annaland, Energy analysis and economic evaluation of two-stage packed-bed CLC configurations for an IGCC power plant, Energy 85 (2015) 489–502, http://dx.doi.org/10.1016/j.energy.2015.03.063.
[17] M.A. San Pio, I. Roghair, F. Gallucci, M. van Sint Annaland, Investigation on the decrease in the reduction rate of oxygen carriers for chemical looping combustion, Powder Technol. 301 (2016), http://dx.doi.org/10.1016/j.powtec.2016.06.031.
[18] M.A. San Pio, F. Gallucci, I. Roghair, V.M Sint Annaland, On the mechanism controlling the redox kinetics of Cu-based oxygen carriers, Chem. Eng. Res. Des. (2017).
[19] S.R. Son, K.S. Go, S.D. Kim, Thermogravimetric analysis of copper oxide for chemical-looping hydrogen generation, Ind. Eng. Chem. Res. 48 (2009) 380–387, http://dx.doi.org/10.1021/ie800174c.
[20] I. Adánez-Rubio, P. Gayán, F. García-Labiano, L.F. de Diego, J. Adánez, A. Abad, Development of CuO-based oxygen-carrier materials suitable for chemical-looping with oxygen uncoupling (CLOU) process, Energy Procedia 4 (2011) 417–424, http://dx.doi.org/10.1016/j.egypro.2011.01.070.
[21] L.F. de Diego Poza, P. Gayán Sanz, F. García Labiano, J. Celaya Romeo, A. Abad Secades, J. Adánez Elorza, Impregnated CuO/Al2O3 oxygen carriers for chemical-looping combustion: avoiding fluidized bed agglomeration, 2005.
[22] A. Abad, J. Adánez, F. García-Labiano, L.F. de Diego, P. Gayán, Modeling of the chemical-looping combustion of methane using a Cu-based oxygen-carrier, Combust. Flame 157 (2010) 602–615, http://dx.doi.org/10.1016/j.combustflame.2009.10.010.
[23] H.P. Hamers, F. Gallucci, P.D. Cobden, E. Kimball, M. Van Sint Annaland, CLC in packed beds using syngas and CuO/Al2O3: model description and experimental validation, Appl. Energy 119 (2014), http://dx.doi.org/10.1016/j.apenergy.2013.12.053.
[24] L. Guo, H. Zhao, K. Wang, D. Mei, Z. Ma, C. Zheng, Reduction kinetics analysis of sol–gel-derived CuO/CuAl2O4 oxygen carrier for chemical looping with oxygen uncoupling, J. Therm. Anal. Calorim. 123 (2016) 745–756, http://dx.doi.org/10.1007/s10973-015-4904-6.
[25] W. Hu, F. Donat, S.A. Scott, J.S. Dennis, The interaction between CuO and Al 2 O 3 and the reactivity of copper aluminates below 1000 C and their implication on the use of the Cu–Al–O system for oxygen storage and production, R. Soc. Chem. (2016).
[26] M.A. San Pio, M. Martini, F. Gallucci, I. Roghair, M. van Sint Annaland, Kinetics of CuO/SiO2 and CuO/Al2O3 oxygen carriers for chemical looping combustion, Chem. Eng. Sci. (2017).
[27] J. Smit, M. Van Sint Annaland, J.A.M. Kuipers, Grid adaptation with WENO schemes for non-uniform grids to solve convection-dominated partial differential equations, Chem. Eng. Sci. 60 (2005) 2609–2619.
[28] D. Vortmeyer, R. Berninger, Comments on the paper, theoretical prediction of effective heat transfer parameters in packed beds by Anthony Dixon and D. L. Cresswell, AIChE J. 28 (1982) 508–510.
[29] R. Bauer, E.U. Schluender, Effective radial thermal conductivity of packings in gas flow, part II: thermal conductivity of the packing fraction without gas flow, 18 (1978) 189–204.
[30] D.J. Gunn, M.A. Misbah, Bayesian estimation of heat transport parameters in fixed beds, Int. J. Heat Mass Transf. 36 (1993) 2209–2221.
[31] D.J. Gunn, Transfer of heat or mass to particles in fixed and fluidised beds, Int. J. Heat Mass Transf. 21 (1978) 467–476.
[32] M.F. Edwards, J.F. Richardson, Gas dispersion in packed beds, Chem. Eng. J. 23 (1968) 109–123.
[33] S. Noorman, F. Gallucci, M. Van Sint Annaland, J.A.M. Kuipers, A theoretical investigation of CLC in packed beds. Part 1: particle model, Chem. Eng. J. 167 (2011), http://dx.doi.org/10.1016/j.cej.2010.12.068.
[34] R. Taylor, R. Krishna, Multicomponent Mass Transfer, Wiley, 1993.
[35] Prof.-Dr. Ing. Ihsan Barin, Thermochemical Data of Pure Substances, Wiley-VCH Verlag GmbH, Weinheim, Germany, 1995. doi:10.1002/9783527619825.
[36] F. García-Labiano, L.F. de Diego, J. Adánez, A. Abad, P. Gayán, Temperature variations in the oxygen carrier particles during their reduction and oxidation in a chemical-looping combustion system, Chem. Eng. Sci. 60 (2005) 851–862, http://dx.doi.org/10.1016/j.ces.2004.09.049.
[37] T.E. Daubert, Data compilation tables of properties of pure compounds, Design Institute for Physical Property Data, American Institute of Chemical Engineers, New York, N.Y. (345 E. 47th St., New York 10017) 1985.
[38] T.P. Tiemersma, A.S. Chaudhari, F. Gallucci, J.A.M. Kuipers, M. van Sint, Annaland, Integrated autothermal oxidative coupling and steam reforming of methane. Part 1: design of a dual-function catalyst particle, Chem. Eng. Sci. 82 (2012) 200–214.
[39] M.A. San Pio, F. Gallucci, I. Roghair, M. van Sint, Annaland, Gas-solids kinetics of CuO/Al2O3 as an oxygen carrier for high-pressure chemical looping processes: the influence of the total pressure, Int. J. Hydrogen Energy (2017), http://dx.doi.org/10.1016/j.ijhydene.2017.03.176.
[40] V. Spallina, P. Chiesa, E. Martelli, F. Gallucci, M.C. Romano, G. Lozza, et al., Reactor design and operation strategies for a large-scale packed-bed CLC power plant with coal syngas, Int. J. Greenhouse Gas Control. 36 (2015) 34–50, http://dx.doi.org/10.1016/j.ijggc.2015.01.025.